

Mode Dispersion in Photonic Crystal Organic Light-Emitting Diodes

Xiangyu Fu, Cheng Peng, Monica Samal, Nilesh Barange, Yi-An Chen, Dong-Hun Shin, Yash Mehta, Adam Rozelle, Chih-Hao Chang, and Franky So*

Cite This: *ACS Appl. Electron. Mater.* 2020, 2, 1759–1767

Read Online

ACCESS |



Metrics & More



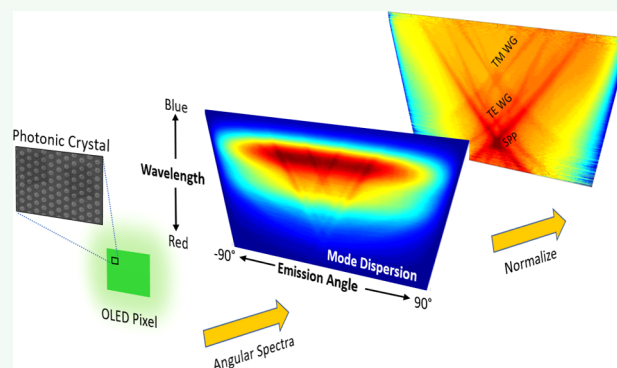
Article Recommendations



Supporting Information

ABSTRACT: Similar to an electronic lattice determining the motion of electrons in solids, photonic crystals (PhCs) are periodic photonic nanostructures that determine the propagation of photons. By incorporating PhCs into organic light-emitting diodes (OLEDs), the device efficiency and emission spectra can be modified, which can be explained and predicted by the mode dispersion. In this work, we experimentally measure the mode dispersion of 1-D and 2-D PhC OLEDs at different azimuthal angles with angle-resolved electroluminescence spectra. The results are explained using an intuitive geometry approach, which shifts and slices the cone-shaped optical modes to obtain the mode dispersion of PhC OLEDs. We note that the weak cavity mode and a narrow photonic band gap are visible only after eliminating the intrinsic emitter spectrum in the air mode dispersion. In the end, we discuss the implication of mode dispersion on the OLED light extraction.

KEYWORDS: OLED, photonic crystal, optical modes, photonic band gap, light extraction



INTRODUCTION

In the past 20 years, organic light-emitting diodes (OLEDs) have received intensive research interest and great progress has been made in their applications for displays and lighting. From the optical aspect, a typical bottom-emitting OLED is a thin-film microcavity formed between the metal cathode and the anode/substrate interface. Its cavity length is determined by the thickness of the organic layers and the transparent ITO anode, which is often in the same order of the visible light wavelength. Due to the cavity effect, around 50% of the photons can escape the thin films and form the substrate mode and air mode, and the rest are coupled to the waveguide modes and surface plasmon polariton (SPP) modes.¹

In a conventional OLED, waveguide and SPP modes can propagate within the thin films for several microns before being absorbed by the metal cathode.² By introducing nanostructured dielectric perturbation to the thin films, the propagation of waveguide and SPP modes can be disrupted or inhibited,³ allowing us to control the optical modes of an OLED.⁴ Structures with dielectric perturbation in the same length scale of the photon wavelength are called photonic crystals (PhCs).^{5,6} One-dimensional (1-D) and two-dimensional (2-D) PhCs are well studied for their simplicity of fabrication.

Over the years, PhCs have been incorporated in OLEDs (PhC OLEDs) to enhance the outcoupling efficiency^{7–11} or to control the emission profile.^{12,13} In both cases, photons trapped in OLEDs are extracted by the PhC through Bragg diffraction. As a result, the air mode of a PhC OLED contains

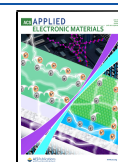
diffraction features corresponding to the extracted waveguide mode and SPP mode. To directly measure the extracted optical modes in the air mode, one can resort to the angle-resolved electroluminescence spectra (ARES) measurements.^{14–16} The air mode can be derived from the ARES data obtained from measurements at all of the emission angles, and therefore it carries a great amount of information on the optical characteristics of the PhC. Several groups have measured ARES on 1-D PhC (i.e., 1-D grating) OLEDs perpendicular to the grating grooves, and the mode dispersion showed an excellent agreement with the optical simulation results.^{16,17} However, this is only one of the special cases and the results cannot be used to fully characterize the 1-D PhC OLED or be generalized for 2-D PhC OLEDs.

Herein, we use ARES to measure the mode dispersion in a conventional planar OLED, a 1-D PhC OLED, and a 2-D PhC OLED having a hexagonal lattice. We demonstrate that the mode dispersion can be normalized to eliminate the emitter emission characteristics and observe the cavity effect in a planar OLED. We then use simple mathematical methods to demonstrate that the full-azimuthal-angle mode dispersion of a

Received: April 22, 2020

Accepted: June 3, 2020

Published: June 3, 2020



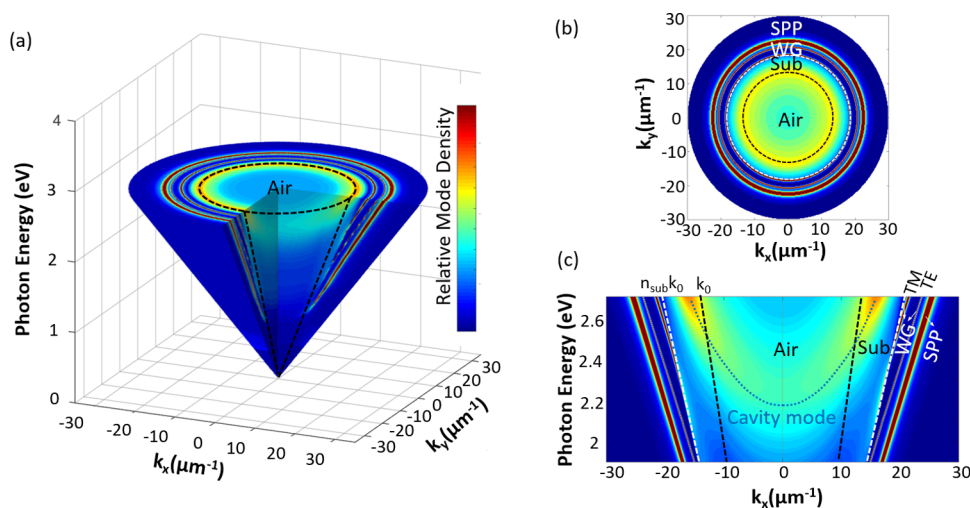


Figure 1. (a) Simulated mode distribution for an isotropic planar OLED device. A quarter of the 3-D shape is open to show the cross section. (b) Far-field emission pattern at a photon energy of 2.6 eV. (c) Mode dispersion along the k_x axis between 1.9 and 2.7 eV. The black dashed lines denote the boundaries of air mode (Air), and the white dashed lines denote the boundaries of the substrate mode (Sub). The two waveguide modes (WG) are denoted as TM and TE modes, respectively.

1-D PhC OLED can be fitted as hyperbolic curves. We also treat the hexagonal 2-D PhC as three sets of 1-D gratings and successfully explain its diffraction properties and their impact on light extraction.

OPTICAL MODES IN OLED

The mode density ($D_{\text{mode}}(E, \vec{k})$) of an OLED device describes the density of photonic states as a function of the photon energy E and the wavevector \vec{k} . Herein, $E = \frac{hc}{\lambda}$ and $k = \frac{2\pi n_{\text{org}}}{\lambda} = n_{\text{org}} k_0$, where h is the Planck constant, c is the speed of light in vacuum, λ is the wavelength of the photon, n_{org} is the refractive index of the emitting layer, and k_0 is the wavevector magnitude of a photon traveling in air. Because \vec{k} is a vector with a fixed magnitude associated with the photon energy, we can represent \vec{k} by its projection in the substrate plane, known as the in-plane wavevector $k_{\text{a||}}$. The magnitude of $k_{\text{a||}}$ provides information on the propagation angle as well as the medium where the wave propagates such that we can use it to construct the optical mode dispersion diagram.¹⁹ The air mode ($k_{\text{a||}} \leq k_0$) refers to the photons that can escape the OLED device. The substrate mode ($k_0 < k_{\text{a||}} \leq n_{\text{sub}} k_0$) is confined in the substrate due to the total internal reflection (TIR) at the substrate/air interface. The waveguide mode ($n_{\text{sub}} k_0 < k_{\text{a||}} \leq n_{\text{org}} k_0$) is confined in the high refractive index organic layer or the ITO layer due to TIR at the ITO/substrate interface and reflection at the metal electrode, and the SPP mode ($k_{\text{a||}} > n_{\text{org}} k_0$) is confined to the interface between the metal electrode and the adjacent organic layer.

In this work, the mode dispersion of our OLED is simulated using Setfos 4.6, which is a commercial optical tool widely used in the OLED industry.²⁰ It uses the oscillating dipole model to simulate the emitter radiative decay and the transfer matrix method to simulate the optical modes and emission properties in a multilayer structure.²¹ We first consider a bottom-emitting device of which the structure is described in the Methods section. The optical mode in this OLED can be visualized with a 4-D (3-D + color) plot, where E is represented by the z axis, $k_{\text{a||}}$ is represented by the x - y plane, and the mode density is represented by the color scale (Figure 1a). Due to the

azimuthal symmetry of the OLED, the air mode is shaped like a cone (hence the name “air cone”). Because of the larger value of the in-plane wavevector, the substrate mode, waveguide modes, and SPP modes are cone shells located outside of the air cone. In practice, it is difficult to visualize a 4-D plot. Instead, we can take a horizontal slice and obtain a far-field emission (FFE) plot, which describes the mode distribution in the x - y plane for a specific photon energy (Figure 1b). Alternatively, we can take a vertical slice containing the origin point and obtain the mode dispersion plot, which describes the mode dispersion along one $k_{\text{a||}}$ direction across a range of photon energies (Figure 1c). In the mode dispersion, the air mode and substrate mode intensity maximum is of parabolic shape as a result of the cavity effect.²² Outside the substrate boundary, we observe one TM waveguide mode, one TE waveguide mode, and one SPP mode. These trapped modes are discrete, and their dispersions are almost linear with the in-plane wavevector within the visible spectrum.

When the electroluminescence (EL) spectrum of the emitter $EL_0(E)$ is taken into consideration, the photonic modes are populated accordingly, and the resulting photon density is given by $P_{\text{mode}}(E, k_{\text{a||}}) = EL_0(E) \cdot D_{\text{mode}}(E, k_{\text{a||}})$, where $D_{\text{mode}}(E, k_{\text{a||}})$ is the mode density. Based on the photon density, we can determine the percentage of photons in each mode and calculate the outcoupling efficiency, which is the fraction of the air mode. In the OLED structure described in the Methods section, 30% of the photons are coupled to the air mode, 24% are coupled to the substrate mode, 16% are coupled to the waveguide modes, and 26% are coupled to the SPP mode (Figure S1). We note that the simulated $P_{\text{mode}}(E, k_{\text{a||}})$ shows a higher intensity along the photon energy at the EL intensity maximum, and the effects of the cavity mode are not apparent in the air mode.

Mode Dispersion in Planar OLEDs. A planar OLED device can be considered as a weak Fabry–Perot cavity.²³ Usually, one of the two mirrors is a reflective metal (Al or Ag), and the other mirror is the ITO/glass interface or a thin metal electrode. In this paper, we consider a conventional glass/ITO/organic layers/Al structure. Photons generated in the emitting layer resonate between the strong reflective metal

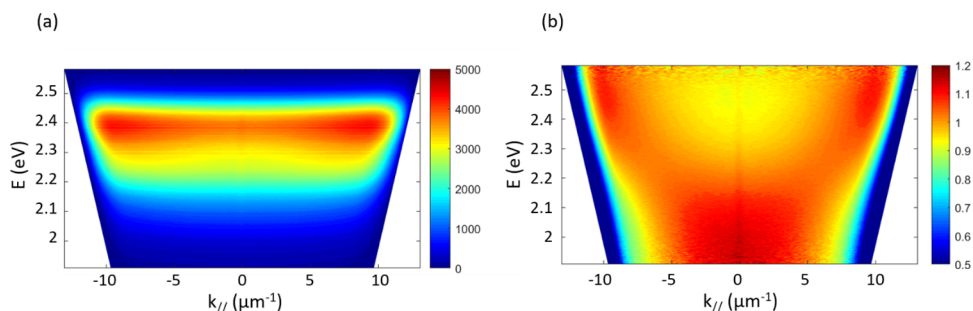


Figure 2. (a) Measured air mode of a planar OLED. (b) Normalized air mode that eliminates the influence from the EL spectrum line shape.

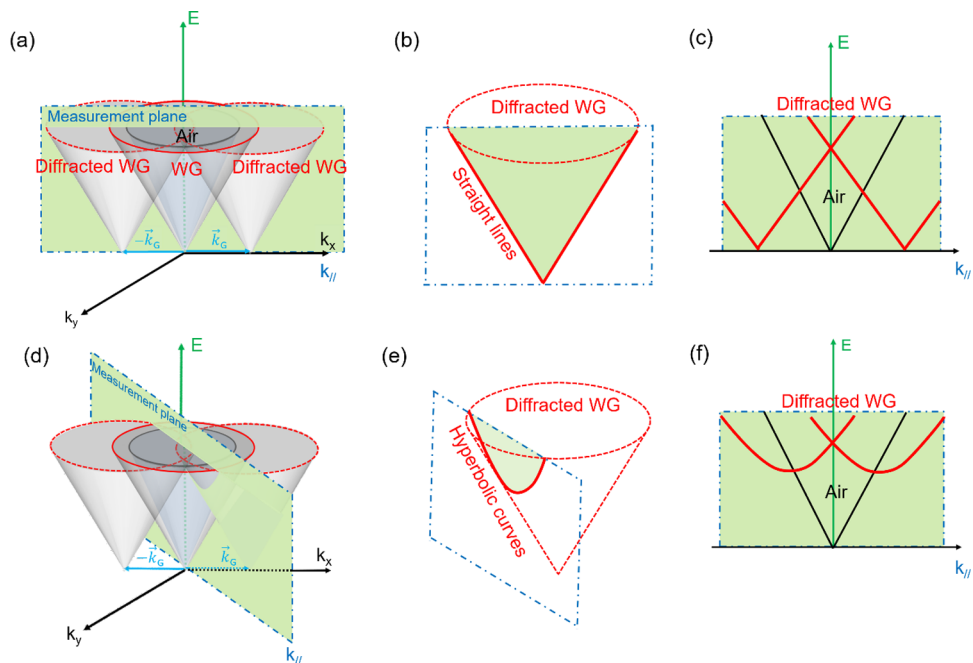


Figure 3. (a) Schematic drawing of the simplified 3-D optical modes consisting of the air mode and a waveguide mode (WG). The waveguide mode is diffracted by \vec{k}_G and $-\vec{k}_G$ to form the two diffracted WG modes. The green planes represent the measurement plane containing the in-plane wavevector $\vec{k}_{a\parallel}$. (b) Corresponding conic sections through one of the diffracted waveguide modes. (c) Measured mode dispersion containing two diffraction features that are straight lines. (d–f) Same schematic drawings but the measurement plane is not along the \vec{k}_G direction, resulting in two hyperbolic diffraction features.

electrode ($R = 85\%$) and the weak reflective ITO/glass interface ($R = 2\%$). Due to the interference, photons having wavelengths and propagation angles satisfying the constructive interference conditions are intensified resulting in a cavity mode. The cavity mode affects the OLED outcoupling efficiency, intensity profile, and angular spectral characteristics.²⁴

We fabricated a planar bottom-emitting OLED and measured its air mode photon density $P_{\text{air}}(E, k_{a\parallel})$ using ARES (Figure S2). The measured air mode is shown in Figure 2a. At each photon energy, the EL intensity appears to be uniform across most $k_{a\parallel}$ values, indicating that the emission profile is close to Lambertian. Note that the photon density maximum is observed at $E = 2.4$ eV, corresponding to the emission peak of the green emitter Ir(ppy)₂(acac) at 520 nm. Herein, the cavity mode is overshadowed by the influence of the emitter spectrum. To directly observe the cavity mode, we can normalize the air mode photon density $P_{\text{air}}(E, k_{a\parallel})$ by the intrinsic EL spectrum $EL_0(E)$ and obtain $D_{\text{air}}(E, k)$. However, to obtain $EL_0(E)$, we either have to precisely model the planar device structure to fit the angular emission profile²⁵ or make an

approximation using the photoluminescence (PL) spectrum.¹⁵ The first approach is only accurate for planar OLEDs with a known device structure, and the second approach neglects the effect of the injected carriers and the location of the recombination zone. In this work, we adopt a different strategy: instead of measuring $EL_0(E)$, we eliminate its effect by normalizing $P_{\text{air}}(E, k_{a\parallel})$ with the average photon density $\overline{P_{\text{air}}(E_0)}$ within each photon energy. This process yields the normalized air mode density $\hat{D}_{\text{air}}(E_0, k_{a\parallel})$

$$\begin{aligned} \frac{P_{\text{air}}(E_0, k_{a\parallel})}{\overline{P_{\text{air}}(E_0)}} &= \frac{EL_0(E_0) \cdot D_{\text{air}}(E_0, k_{a\parallel})}{EL_0(E_0) \cdot \frac{1}{\Delta k_{a\parallel}} \int D_{\text{air}}(E_0, k_{a\parallel}) dk_{a\parallel}} \\ &= \frac{D_{\text{air}}(E_0, k_{a\parallel})}{\overline{D_{\text{air}}(E_0)}} = \hat{D}_{\text{air}}(E_0, k_{a\parallel}) \end{aligned} \quad (1)$$

where $\Delta k_{a\parallel}$ is the integration range of $k_{a\parallel}$. $\hat{D}_{\text{air}}(E_0, k_{a\parallel})$ represents the relative photon distribution in the air mode and is independent on $EL_0(E)$.

We use this approach and plot the normalized air mode of the planar OLED in Figure 2b. After eliminating the effects of

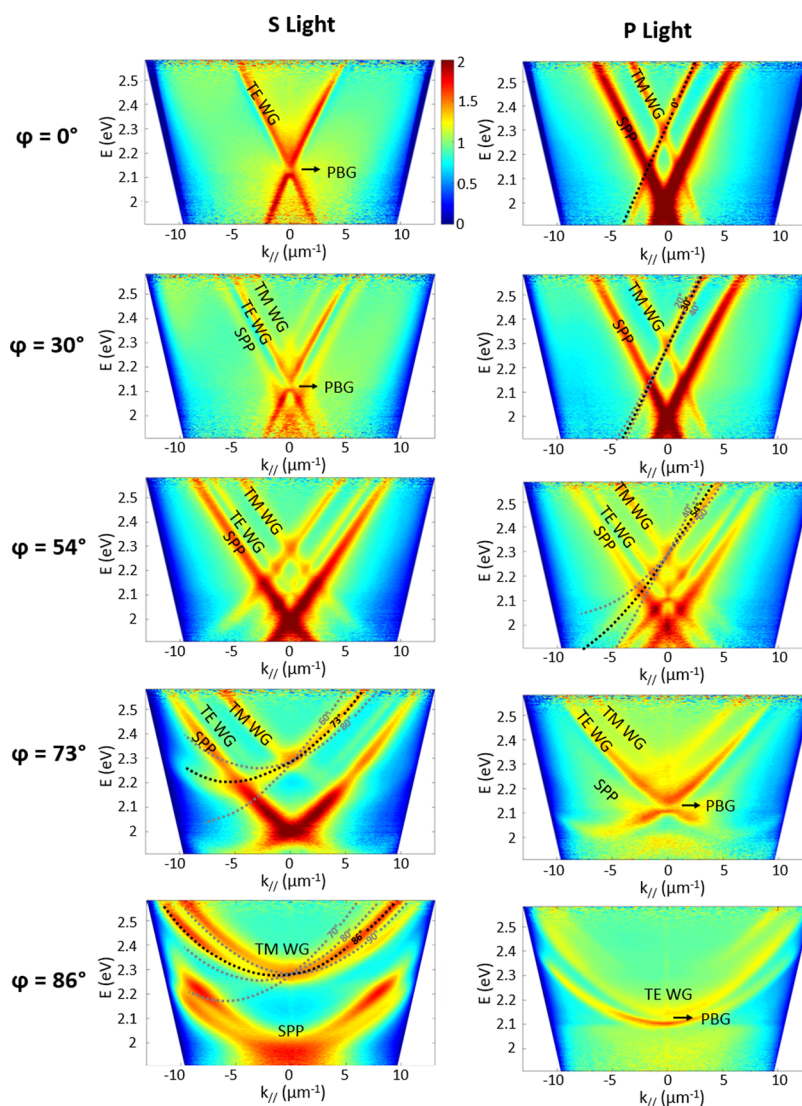


Figure 4. Normalized air mode dispersion measured for a 1-D PhC OLED at $\varphi = 0, 30, 54, 73,$ and 86° for both S light and P light. The φ values are fitted with hyperbolic curves, shown as dotted lines. The origin of the diffraction features is labeled as TE waveguide mode (TE WG), TM waveguide mode (TM WG), and SPP mode (SPP). The arrow indicates the photonic band gap (PBG) in the TE WG.

$EL_0(E)$, we can clearly see the distinct parabolic feature corresponding to the cavity mode. Along the cavity mode, the cavity emission is intensified from the constructive interference resulting in $\hat{D}_{\text{air}}(E_0, k_{\text{a||}}) > 1$. At $\theta = 0^\circ$, the cavity mode peak is at 630 nm; as θ increases, the cavity mode shifts toward shorter wavelengths; at $\theta = 50^\circ$, the cavity mode peak is at 490 nm. The blue-shift phenomenon at larger viewing angles is in good agreement with the previous reports.^{26,27}

Mode Dispersion in 1-D Photonic Crystal OLEDs. As explained previously, photons trapped in the waveguide and SPP modes can be extracted using photonic crystals.^{28,29} The periodically corrugated interfaces in a photonic crystal act as the diffraction gratings. For a photonic crystal having a periodicity of Λ , the magnitude of the grating vector is $k_G = \frac{2\pi}{\Lambda}$. When photons are incident on the photonic crystal, their propagation angles are changed due to Bragg diffraction. The in-plane wavevector of the diffracted photons $\vec{k}'_{\text{a||}}$ can be calculated as $\vec{k}'_{\text{a||}} = \vec{k}_{\text{a||}} \pm m \cdot \vec{k}_G$, where $\vec{k}_{\text{a||}}$ is the in-plane wavevector of the trapped photons, and m is the diffraction order. When $k'_{\text{a||}}$ is smaller than k_0 , the trapped photons are

extracted into the air mode. Here, we use photonic crystals with a subwavelength periodicity such that the first-order diffraction of the trapped photons can be extracted to the air mode. With shallow photonic crystal patterns and small refractive index contrast, the corrugated interfaces in the PhC OLED can be treated as refractive index perturbations in a planar OLED device.¹⁷ Therefore, we can use the mode dispersion of a planar OLED and shift its optical modes by \vec{k}_G to produce the mode dispersion of a PhC OLED. Later we will show that this is a valid assumption from the measurement results.

To understand the optical mode composition in a PhC OLED, we first examine the simple case with a 1-D photonic crystal, i.e., a 1-D grating. Because the 1-D grating is anisotropic in the x - y plane, the mode dispersion is dependent on the measurement plane, i.e., the device orientation angle φ during the ARES measurements. So far, measurements on 1-D PhC OLEDs have only been made for the mode dispersion at $\varphi = 0^\circ$, where the measurement plane is parallel to \vec{k}_G (and perpendicular to the grating grooves).^{17,18,30} We use schematic drawings to explain the diffracted mode dispersion in Figure 3.

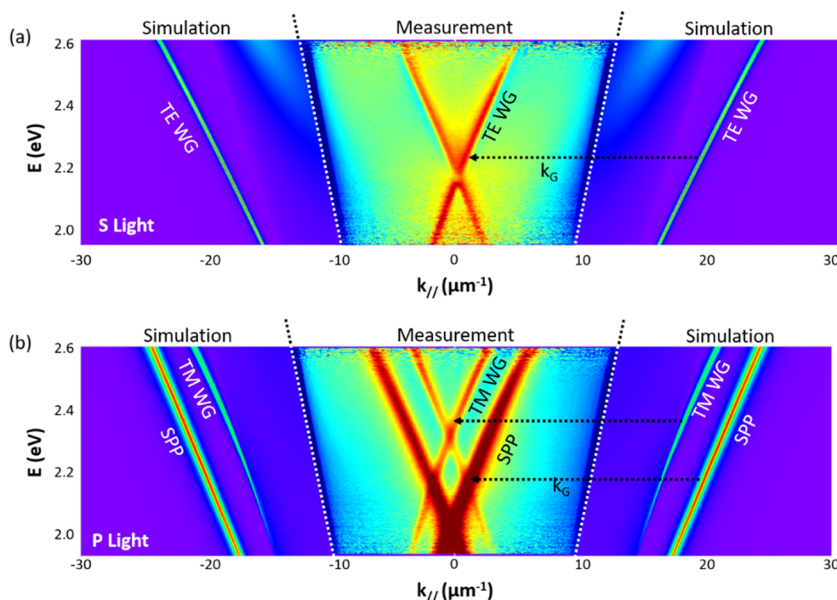


Figure 5. Assignment of measured diffraction features to the optical modes based on the optical simulation, both in (a) S polarization and (b) P polarization. The white dotted lines are the air cone boundaries. To the center of the air cone is the normalized air mode measured on a 1-D photonic crystal OLED at $\varphi = 0^\circ$. To the left and right of the air cone is the simulated mode density based on a planar OLED with the same layer structure as the photonic crystal OLED. The black dotted arrows represent the grating vector k_G of the 1-D grating, which has a periodicity of 350 nm.

For simplicity, we only consider the air mode and one waveguide mode. Within the wavelength range of interest, we can assume that the waveguide mode has a linear dispersion relation and the 3-D waveguide mode is a cone shell. When the waveguide mode is diffracted by the 1-D grating, it forms two diffracted waveguide modes that are shifted from the original waveguide cone by k_G and $-k_G$. In this case, the measurement plane dissects through the center of the diffracted waveguide modes, and the diffracted waveguide features are straight lines (Figure 3a–c); to be more precise, the diffracted mode is shifted in parallel by k_G from the original mode, with the shape of the mode dispersion being preserved. When the measurement plane is not along k_G , it dissects the diffracted waveguide mode off the cone center, with the cross section of the diffracted waveguide mode hyperbolic in shape (Figure 3d–f). The shape of the hyperbolic curve depends on the φ angle and can be explained with conic sections. We note that due to symmetry, the mode dispersion of a 1-D PhC OLED is mirrored, and the diffracted modes intercept at the same photon energy at $k_{a||} = 0$ for all of the φ angles.

We fabricated an OLED on a 1-D grating with a 350 nm periodicity and measured its normalized air mode dispersion at different φ for both S and P polarized lights (Figure 4). When $\varphi = 0^\circ$, we observed a clear separation of the polarization of the diffraction features. Based on the optical mode simulation of a planar OLED, we assign these features to the diffracted waveguide and SPP modes determined by the magnitude of $k_{a||}$ (Figure 5). The good agreement between the measured diffraction features and the simulated mode dispersion of a planar OLED confirms that the shallow corrugation in a PhC OLED can be treated as perturbations in a planar OLED.

As φ increases, the linear diffraction features start bending and morphed into hyperbolic curves. This is confirmed by fitting the diffracted TM waveguide mode dispersion using conic section equations and varying the φ parameter (method described in Figure S6). The calculation shows very good

agreement with the measurement results. Between $\varphi = 0$ and 40° , the diffracted TM waveguide mode dispersion barely changed. When φ increases over 40° , the dispersion starts bending notably following the hyperbolic curve. Note that the interception at $k_{a||} = 0$ remains constant that acts as an anchor point when the mode dispersion shifts, which is useful for labeling the origin of the diffraction features.

We also observe the mixing of polarizations, where diffraction features from TE waveguide, TM waveguide mode, and SPP mode can be seen in both S and P polarizations. At $\varphi = 86^\circ$, we observe an almost complete inversion of the polarization of the diffraction feature from the original mode. This is due to the angle φ between the polarization of the light and the polarizer axis, which results in a distribution of light density in both polarizations in the form of $\cos^2\varphi$, $\sin^2\varphi$.³¹

Another observation is the formation of photonic band gap (PBG) in the TE waveguide mode. For S light at $\varphi = 0$ and 30° , we can observe an anticrossing between the two diffracted TE waveguide modes at the air cone center, which indicates the formation of a PBG. The PBG is more visible for P light at $\varphi = 73$ and 86° , where we can see that the TE waveguide mode splits into two bands, creating a PBG at the air cone center between 2.11 (587 nm) and 2.13 eV (582 nm). Because the TE waveguide mode is located in the ITO anode, we attribute the PBG formation to the photonic crystal formed between ITO and glass. Because the refractive index contrast between the two materials is around 0.5, the PBG width is only 5 nm.

We note that PBG in a 1-D PhC has been observed in polymer lasers under optical pumping.^{32,33} In such devices, the TE waveguide mode emission is intensified by the optical resonance; therefore, its PBG is easily recognizable. For PhC OLEDs, however, the PBG is overshadowed by the air mode background and emitter EL profile $EL_0(E)$ (Figure S6). By normalizing the air mode, we are able to eliminate the influence of $EL_0(E)$ and observe the formation of the PBG.

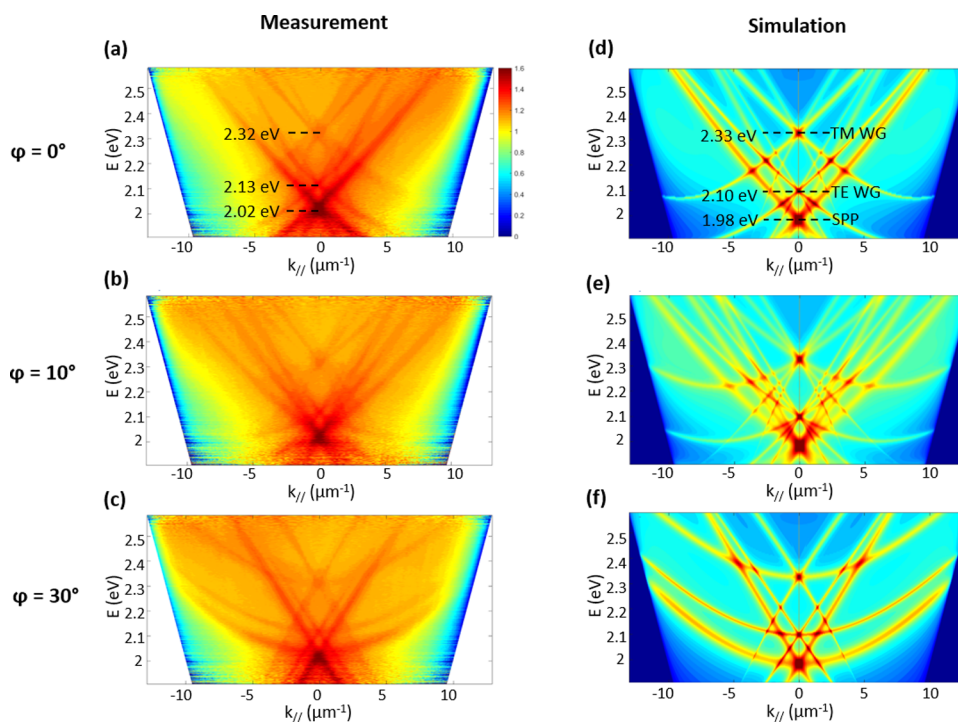


Figure 6. Normalized air mode measured for a photonic crystal OLED at (a) $\varphi = 0^\circ$, (b) $\varphi = 10^\circ$, and (c) $\varphi = 30^\circ$. The simulated mode dispersion plots at the same azimuthal angles are shown in (d–f). The origin of the diffraction features is labeled in (d) as TM waveguide mode (TM WG), TE waveguide mode (TE WG), and SPP mode (SPP).

Mode Dispersion in 2-D Photonic Crystal OLEDs.

Because a 1-D photonic crystal has two opposing \vec{k}_G , it only forms two sets of diffracted modes. Therefore, the portion of diffracted modes within the air cone is limited, and only light propagating within a small range of φ can be extracted. A 2-D photonic crystal has index perturbation in more than one direction, so it can have more than one set of \vec{k}_G , which allows light propagating in a broader range of φ to be extracted. In this study, we fabricate a 2-D PhC OLED on a substrate having a hexagonal photonic crystal pattern (Figure S7). For the light diffraction perspective, such a hexagonal photonic crystal can be treated as three identical 1-D gratings oriented at an angle of 60° from each other; thus, it has 6 \vec{k}_G . Using the perturbation treatment described previously, we can simulate the mode dispersion in a photonic crystal OLED by shifting the optical modes in a planar OLED by \vec{k}_G in six directions. The simulation details are described in the Supporting Information.

The measured normalized air modes for the 2-D photonic crystal OLED at $\varphi = 0, 10,$ and 30° are shown in Figure 6a–c, and the corresponding simulation results are shown in Figure 6d–f. We first note the measured and simulated mode dispersions are in good agreement, confirming the assumption that a hexagonal photonic crystal can be treated as a perturbation of three 1-D gratings in light diffraction. We can observe the linear and hyperbolic features corresponding to the extracted waveguide and SPP modes. As was discussed in the 1-D grating case, the linear features observed at $\varphi = 0$ and 30° are present when the measurement plane is along one \vec{k}_G ; the hyperbolic features are present when the measurement plane is not along any \vec{k}_G . In each plot, we can see three sets of diffraction features intercepting at the center of the air cone at the same photon energy. This is due to the symmetry of the photonic crystal pattern and the diffraction features from the

same optical mode intercept at a photon energy E_0 satisfying the condition that $k_{\text{SPP/WG}}(E_0) = k_G$. In the measurement results, the intercepting photon energies (wavelengths) are 2.32 (534 nm), 2.13 (582 nm), and 2.02 eV (614 nm), which correspond to the simulation results for the TM waveguide mode, TE waveguide mode, and SPP mode at 2.33 (532 nm), 2.10 (590 nm), and 1.98 eV (625 nm), respectively. The difference between the simulation and the measurement results is less than 0.05 eV.

To better visualize the mode diffraction from the hexagonal lattice, we measured the FFE pattern of the 2-D PhC OLED by aligning the measuring plane to one of the \vec{k}_G and measuring the mode dispersion within a 30° section of the air cone at a step of 2° . We then assume the hexagonal symmetry to produce the air mode dispersion. We dissect the measured air mode and obtain the FFE patterns at wavelengths of 520, 560, and 600 nm as shown in Figure 7a–c. The results are compared to the simulated FFE patterns, as shown in Figure 7d–f. From the FFE pattern at 520 nm, we can see two distinct lotus flower patterns, each having features of six arc-shaped diffraction patterns, corresponding to the diffracted TM waveguide mode and SPP mode. The TE waveguide mode is indistinguishable from the SPP mode due to their close proximity in the $k_{\text{a||}}$ value, and the strong intensity of the SPP mode and the narrow line shape of the TE waveguide mode. As the wavelength increases to 560 and 600 nm, the diffraction features from the SPP mode become dominant, and the TM waveguide patterns become less visible. In addition, the SPP mode arcs move toward the center of the air mode as the wavelength changes. This is because k_{SPP} is wavelength-dependent while k_G is wavelength-independent. Therefore, the resulting $\vec{k}'_{\text{SPP}} = \vec{k}_{\text{SPP}} - \vec{k}_G$ is dependent on the wavelength of the emitted light. We note that in the measured FFE plots, the diffraction features become invisible near the edge of air mode.

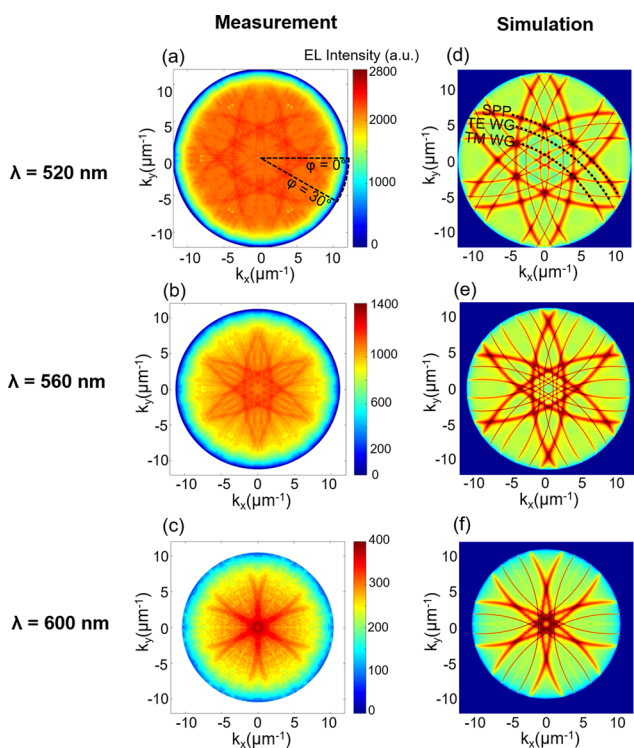


Figure 7. Measured far-field emission pattern of a photonic crystal OLED with a hexagonal photonic crystal pattern at the wavelength of (a) 520, (b) 560, and (c) 600 nm. At 520 nm, the black dashed lines mark the section of air mode measured with ARES. The simulated far-field emission plots at each wavelength are shown in (d–f). The black dashed lines mark the arc-shaped diffraction features corresponding to TM waveguide mode (TM WG), TE waveguide mode (TE WG), and SPP mode (SPP).

This is because the projected area of the OLED decreases with φ by the cosine law; at glancing angles, the area becomes very small and its alignment to the optical fiber becomes difficult.

From the efficiency aspect, the 2-D PhC OLED shows a current efficiency of 120 cd/A and an EQE of 33%, which is 32 and 22% higher than the planar OLED, respectively (Figure S7). We compare the intensity of the extracted modes in the ARES measurements and correlate the current efficiency and EQE enhancement to each mode. The EQE value corresponds to the overall photon density at all angles. Because the SPP mode diffraction is the strongest across all wavelengths and angles, it contributes the most to the EQE enhancement. On the other hand, the current efficiency is correlated with the forward light intensity and the human eye response, which is the strongest at 555 nm. Although the extracted SPP mode has the strongest contribution, it enhances the forward light intensity at around 617 nm. In comparison, the extracted TM waveguide enhances at 534 nm, close to the $\text{Ir}(\text{ppy})_2(\text{acac})$ emission peak and the human eye response peak. As a result, the TM waveguide mode ends up contributing the most to the current efficiency enhancement.

The discussion above aims at determining the optical modes in a PhC OLED without quantifying the photon numbers. The absolute photon count is influenced by the ARES setup, including the optics of the system as well as the response of the spectrometer. To quantitatively determine the photon distribution, the ARES setup should be calibrated with a standard wide-spectrum light source with a known emission profile, for example, a Lambertian tungsten light source with a

calibrated spectral power density. This will allow us to quantitatively determine the contribution from each optical mode and estimate the remaining trapped light amount. Another benefit of calibrating the ARES setup is that we can directly use ARES to measure the directional light output and hence determine the current efficiency and EQE. Given that the information regarding the emitted color (e.g., CIE coordinates) is also encoded in the EL spectra, we can obtain most of the optical characteristics of an OLED using ARES measurements.

CONCLUSIONS

In conclusion, we demonstrate direct measurements of the air mode in both planar and PhC OLEDs using ARES and confirmed the results with optical simulation. We characterize the cavity modes in a planar OLED and explain the blue shift in the EL spectrum due to the cavity effect. We explain the mode dispersion of 1-D photonic crystal OLED at different azimuth angles and note the formation of a photonic band gap. We then extend the idea to 2-D photonic crystal OLEDs and successfully explain its mode dispersion by considering the hexagonal lattice as three sets of 1-D gratings. We also demonstrate that ARES can be used to characterize the light extraction in photonic crystal OLEDs. By normalizing the measured air mode, we eliminate the effect from the emitter EL spectrum and reveal the extraction features from Bragg diffraction, trace back the origin of the extracted light, and correlate the efficiency enhancement to each extracted mode. This study showcases ARES as a powerful tool to study the optical properties of an OLED and provide crucial guidelines on the optical design of photonic crystal OLEDs for light extraction.

METHODS

Fabrication of Planar and Photonic Crystal OLED. The device structure of the planar OLED device is ITO (110 nm)/ MoO_x (10 nm)/4,4'-cyclohexylidenebis[*N,N*-bis(4-methylphenyl)benzenamine] (TAPC) (40 nm)/4,4'-bis(*N*-carbazolyl)-1,1'-biphenyl (CBP) (20 nm):7% bis[2-(2-pyridinyl-*N*)phenyl-C](acetylacetonato)iridium(III) ($\text{Ir}(\text{ppy})_2(\text{acac})$)/4,6-bis(3,5-di(pyridin-3-yl)phenyl)-2-methylpyrimidine (B3PYMPM) (10 nm)/4,7-diphenyl-1,10-phenanthroline (Bphen) (50 nm)/ Cs_2CO_3 (2 nm)/Al (100 nm). The ITO layer is sputtered in a Kurt J. Lesker sputter. The rest of the OLED layers are evaporated in a Trovato evaporator system under high vacuum of 5×10^{-7} Torr. The evaporation rate of MoO_x is 0.4 Å/s, $\text{Ir}(\text{ppy})_2(\text{acac})$ is 0.07 Å/s, Cs_2CO_3 is 0.1 Å/s, and Al is 2 Å/s. The other layers are evaporated at 1 Å/s.

For the photonic crystal OLED, we first fabricate a corrugated substrate through soft-imprinting. A perfluoropolyether (PFPE) stamp is used to replicate the photonic crystal pattern from the master mold. The replicated 1-D and 2-D photonic crystal patterns are both 350 nm in periodicity and about 100 nm in depth (Figure S5). The glass substrates are cleaned with a standard ultrasonication procedure in acetone and isopropyl alcohol for 15 min each. Then, a small amount of NOA-81 epoxy (from Norland Products Inc.) is dropcast on the glass substrate. The stamp is pressed on the epoxy to remove air gaps in between. Then, the substrate with the stamp is treated under 365 nm UV light (Jelight UVO cleaner Model 42) for 4 min to cure the epoxy. Afterwards, the stamp is removed to leave behind the corrugated substrate. OLED devices which have the same layer structures as the planar OLED is fabricated on the corrugated substrate.

■ ASSOCIATED CONTENT

SI Supporting Information

The Supporting Information is available free of charge at <https://pubs.acs.org/doi/10.1021/acsaelm.0c00326>.

Optical simulation of the planar and 2-D photonic crystal OLEDs, direct measurements of the air mode with ARES, simulated and measured planar OLED air mode dispersion, fitting of mode dispersion in 1-D PhC OLED using conic section, comparison of the J - V , current efficiency, EQE and forward EL spectra for the planar and the 2-D PhC OLEDs (PDF)

■ AUTHOR INFORMATION

Corresponding Author

Franky So – Department of Material Science and Engineering, North Carolina State University, Raleigh, North Carolina 27695, United States; orcid.org/0000-0002-8310-677X; Email: fso@ncsu.edu

Authors

Xiangyu Fu – Department of Material Science and Engineering, North Carolina State University, Raleigh, North Carolina 27695, United States

Cheng Peng – Department of Material Science and Engineering, North Carolina State University, Raleigh, North Carolina 27695, United States

Monica Samal – Department of Material Science and Engineering, North Carolina State University, Raleigh, North Carolina 27695, United States

Nilesh Barange – Department of Material Science and Engineering, North Carolina State University, Raleigh, North Carolina 27695, United States

Yi-An Chen – Walker Department of Mechanical Engineering, University of Texas at Austin, Austin, Texas 78712, United States

Dong-Hun Shin – Department of Chemical and Biomolecular Engineering, North Carolina State University, Raleigh, North Carolina 27695, United States

Yash Mehta – Department of Material Science and Engineering, North Carolina State University, Raleigh, North Carolina 27695, United States

Adam Rozelle – Department of Material Science and Engineering, North Carolina State University, Raleigh, North Carolina 27695, United States

Chih-Hao Chang – Walker Department of Mechanical Engineering, University of Texas at Austin, Austin, Texas 78712, United States

Complete contact information is available at: <https://pubs.acs.org/doi/10.1021/acsaelm.0c00326>

Notes

The authors declare no competing financial interest.

■ ACKNOWLEDGMENTS

The authors acknowledge the financial support provided by the Department of Energy Award No. DE-EE0007624.

■ REFERENCES

(1) Meerheim, R.; Furno, M.; Hofmann, S.; Lüssem, B.; Leo, K. Quantification of Energy Loss Mechanisms in Organic Light-Emitting Diodes. *Appl. Phys. Lett.* **2010**, *97*, No. 253305.

(2) Barnes, W. L.; Dereux, A.; Ebbesen, T. W. Surface Plasmon Subwavelength Optics. *Nature* **2003**, *424*, 824–830.

(3) Fujita, M.; Takahashi, S.; Tanaka, Y.; Asano, T.; Noda, S. Simultaneous Inhibition and Redistribution of Spontaneous Light Emission in Photonic Crystals. *Science* **2005**, *308*, 1296–1298.

(4) Hong, K.; Yu, H. K.; Lee, I.; Kim, K.; Kim, S.; Lee, J. L. Enhanced Light Out-Coupling of Organic Light-Emitting Diodes: Spontaneously Formed Nanofacet-Structured MgO as a Refractive Index Modulation Layer. *Adv. Mater.* **2010**, *22*, 4890–4894.

(5) Yablonovitch, E. Photonic Band-Gap Structures. *J. Opt. Soc. Am. B* **1993**, *10*, 283–295.

(6) Joannopoulos, J. D.; Villeneuve, P. R.; Fan, S. Photonic Crystals. *Solid State Commun.* **1997**, *102*, 165–173.

(7) Do, Y. R.; Kim, Y. C.; Song, Y. W.; Lee, Y. H. Enhanced Light Extraction Efficiency from Organic Light Emitting Diodes by Insertion of a Two-Dimensional Photonic Crystal Structure. *J. Appl. Phys.* **2004**, *96*, 7629–7636.

(8) Koo, W. H.; Jeong, S. M.; Araoka, F.; Ishikawa, K.; Nishimura, S.; Toyooka, T.; Takezoe, H. Light Extraction from Organic Light-Emitting Diodes Enhanced by Spontaneously Formed Buckles. *Nat. Photonics* **2010**, *4*, 222–226.

(9) Ou, Q. D.; Zhou, L.; Li, Y. Q.; Shen, S.; Chen, J. D.; Li, C.; Wang, Q. K.; Lee, S. T.; Tang, J. X. Extremely Efficient White Organic Light-Emitting Diodes for General Lighting. *Adv. Funct. Mater.* **2014**, *24*, 7249–7256.

(10) Jeon, S.; Lee, J. H.; Jeong, J. H.; Song, Y. S.; Moon, C. K.; Kim, J. J.; Youn, J. R. Vacuum Nanohole Array Embedded Phosphorescent Organic Light Emitting Diodes. *Sci. Rep.* **2015**, *5*, No. 8685.

(11) Shim, Y. S.; Hwang, J. H.; Park, C. H.; Jung, S. G.; Park, Y. W.; Ju, B. K. An Extremely Low-Index Photonic Crystal Layer for Enhanced Light Extraction from Organic Light-Emitting Diodes. *Nanoscale* **2016**, *8*, 4113–4120.

(12) Feng, J.; Okamoto, T.; Kawata, S. Highly Directional Emission via Coupled Surface-Plasmon Tunneling from Electroluminescence in Organic Light-Emitting Devices. *Appl. Phys. Lett.* **2005**, *87*, No. 241109.

(13) Zhang, S.; Turnbull, G. A.; Samuel, I. D. Highly Directional Emission and Beam Steering from Organic Light-Emitting Diodes with a Substrate Diffractive Optical Element. *Adv. Opt. Mater.* **2014**, *2*, 343–347.

(14) Yates, C. J.; Samuel, I. D. W.; Burn, P. L.; Wedge, S.; Barnes, W. L. Surface Plasmon-Polariton Mediated Emission from Phosphorescent Dendrimer Light-Emitting Diodes. *Appl. Phys. Lett.* **2006**, *88*, No. 161105.

(15) David, A.; Meier, C.; Sharma, R.; Diana, F. S.; Denbaars, S. P.; Hu, E.; Nakamura, S.; Weisbuch, C.; Benisty, H. Photonic Bands in Two-Dimensionally Patterned Multimode GaN Waveguides for Light Extraction. *Appl. Phys. Lett.* **2005**, *87*, No. 101107.

(16) Daskalakis, K. S.; Freire-Fernández, F.; Moilanen, A. J.; Van Dijken, S.; Törmä, P. Converting an Organic Light-Emitting Diode from Blue to White with Bragg Modes. *ACS Photonics* **2019**, *6*, 2655–2662.

(17) Schwab, T.; Fuchs, C.; Scholz, R.; Zakhidov, A.; Leo, K.; Gather, M. C. Coherent Mode Coupling in Highly Efficient Top-Emitting OLEDs on Periodically Corrugated Substrates. *Opt. Express* **2014**, *22*, 7524–7537.

(18) Will, P. A.; Schwarz, E. B.; Fuchs, C.; Scholz, R.; Lenk, S.; Reineke, S. Scattering Quantified: Evaluation of Corrugation Induced Outcoupling Concepts in Organic Light-Emitting Diodes. *Org. Electron.* **2018**, *58*, 250–256.

(19) Salehi, A.; Fu, X.; Shin, D. H.; So, F. Recent Advances in OLED Optical Design. *Adv. Funct. Mater.* **2019**, *29*, No. 1808803.

(20) Fluxim, A. G. SETFOS: Semiconducting Emissive Thin Film Optics Simulator Software. <http://www.fluxim.com>.

(21) Penninck, L.; Mladenowski, S.; Neyts, K. The Effects of Planar Metallic Interfaces on the Radiation of Nearby Electrical Dipoles. *J. Opt.* **2010**, *12*, No. 075001.

(22) Zhang, X. L.; Feng, J.; Han, X. C.; Liu, Y. F.; Chen, Q. D.; Song, J. F.; Sun, H. B. Hybrid Tamm Plasmon-Polariton/Microcavity

Modes for White Top-Emitting Organic Light-Emitting Devices. *Optica* **2015**, *2*, 579–584.

(23) Bulović, V.; Khalfin, V. B.; Gu, G.; Burrows, P. E.; Garbuzov, D. Z.; Forrest, S. R. Weak Microcavity Effects in Organic Light-Emitting Devices. *Phys. Rev. B* **1998**, *58*, 3730–3740.

(24) Furno, M.; Meerheim, R.; Thomschke, M.; Hofmann, S.; Lüssem, B.; Leo, K. Outcoupling Efficiency in Small Molecule OLEDs: from Theory to Experiment. *Int. Soc. Opt. Photonics* **2019**, No. 761716.

(25) Wierer, J. J., Jr.; David, A.; Megens, M. M. III-Nitride Photonic-Crystal Light-Emitting Diodes with High Extraction Efficiency. *Nat. Photonics* **2009**, *3*, 163–169.

(26) Liu, C. C.; Liu, S. H.; Tien, K. C.; Hsu, M. H.; Chang, H. W.; Chang, C. K.; Yang, C. J.; Wu, C. C. Microcavity Top-Emitting Organic Light-Emitting Devices Integrated with Diffusers for Simultaneous Enhancement of Efficiencies and Viewing Characteristics. *Appl. Phys. Lett.* **2009**, *94*, No. 103302.

(27) Tan, G.; Lee, J. H.; Lin, S. C.; Zhu, R.; Choi, S. H.; Wu, S. T. Analysis and Optimization on the Angular Color Shift of RGB OLED Displays. *Opt. Express* **2017**, *25*, 33629–33642.

(28) Frischeisen, J.; Niu, Q.; Abdellah, A.; Kinzel, J. B.; Gehlhaar, R.; Scarpa, G.; Adachi, C.; Lugli, P.; Brütting, W. Light Extraction from Surface Plasmons and Waveguide Modes in an Organic Light-Emitting Layer by Nanoimprinted Gratings. *Opt. Express* **2011**, *19*, A7–A19.

(29) Hauss, J.; Bocksrocker, T.; Riedel, B.; Lemmer, U.; Gerken, M. On the Interplay of Waveguide Modes and Leaky Modes in Corrugated OLEDs. *Opt. Express* **2011**, *19*, A851–A858.

(30) Fuchs, C.; Schwab, T.; Roch, T.; Eckardt, S.; Lasagni, A.; Hofmann, S.; Lüssem, B.; Müller-Meskamp, L.; Leo, K.; Gather, M. C.; Scholz, R. Quantitative Allocation of Bragg Scattering Effects in Highly Efficient OLEDs Fabricated on Periodically Corrugated Substrates. *Opt. Express* **2013**, *21*, 16319–16330.

(31) Matioli, E.; Brinkley, S.; Kelchner, K. M.; Hu, Y. L.; Nakamura, S.; DenBaars, S.; Speck, J.; Weisbuch, C. High-Brightness Polarized Light-Emitting Diodes. *Light: Sci. Appl.* **2012**, *1*, No. e22.

(32) Turnbull, G. A.; Andrew, P.; Jory, M. J.; Barnes, W. L.; Samuel, I. D. W. Relationship between Photonic Band Structure and Emission Characteristics of a Polymer Distributed Feedback Laser. *Phys. Rev. B* **2001**, *64*, No. 125122.

(33) Heliotis, G.; Xia, R.; Bradley, D. D. C.; Turnbull, G. A.; Samuel, I. D. W.; Andrew, P.; Barnes, W. L. Blue, Surface-Emitting, Distributed Feedback Polyfluorene Lasers. *Appl. Phys. Lett.* **2003**, *83*, 2118–2120.